SUPPORTING MATERIALS

SUPPLEMENTARY MATERIALS AND METHODS:

Single molecule assay using plain glass and β-casein

Flow chambers were assembled as described in the Methods, but using plain ethanol-boiled cover glass instead of biotin-PEG functionalized glass. The counter glass was PLL-PEG passivated. The chamber was first washed with MT buffer (see Methods) and then equilibrated with rabbit polyclonal anti-α-tubulin antibody (ab18251; Abcam, Cambridge, UK) diluted to 50 μg/ml in MT buffer for 5 min on ice. This antibody binds non-specifically to the glass. After washing the chamber was incubated with Taxol stabilized, Alexa-647 labeled microtubules in MT buffer containing 5 μM Taxol for 5 min at 25 °C. Microtubules not being immobilized on the surface were removed by washing the flow chamber. In the subsequent blocking step the chamber was incubated with β-casein at 0.5 mg/ml in MT buffer for 5 min. For imaging Kin_{401}mGFP in the absence and presence of the rigor kinesin Kin_{401}[T99N]mCherry, we used the same protocol and buffers as described in the Methods. Because of less efficient passivation by β-casein the motor and roadblock concentrations had to be increased 10–20x to obtain similar kinesin landing rates and roadblock decoration as with PEG-biotin coated glass.

Single molecule assay using quantum dot labeled kinesin

Biotinylated kinesin Kin_{401}BCCP (biotin carboxyl carrier protein) was expressed and purified as described elsewhere (1). For labeling with streptavidin-coated quantum dots (Qdot 585, Invitrogen) we mixed Kin_{401}BCCP with quantum dots at 1:1 molar ratio as described in (2). For single molecule imaging we prepared casein-blocked flow chambers as described above. After immobilizing microtubules to the glass surface and a subsequent casein blocking step, 20 nM rigor kinesin Kin_{401}[T99N]mGFP in assay buffer (see Methods) was added to the flow cell for 5 min. Then, for the final sample the mixture of Kin_{401}BCCP and Qdots was flowed in and imaged as described in Methods.

Detection of pauses and stops

Typical tracks of moving kinesins exhibit frame-to-frame vector displacements in ‘forward’ direction within our exposure time, while apparently non-moving signal spots show instantaneous reversal of their vector displacement around an average steady position (stochasticity of noise, see Fig. 5 in main paper). Thus, we decided to scan the tracks for two discrete properties of frame-to-frame displacement: (a) extreme change, even reversal in movement direction, and (b) forward displacements below the accuracy limit (Fig. S3 A).

For each tracked run we first determined the main axis of movement by calculating the second moments of the track positions $p_i \equiv p(t_i) = (x_i, y_i)$ according to

$$I_x = \sum_i y_i^2 \quad , \quad I_y = \sum_i x_i^2 \quad , \quad I_{xy} = \sum_i x_i y_i \qquad \text{[S1]}$$

Very long tracks were divided into overlapping sections involving maximally twenty consecutive positions, and the second moments of these sections were calculated separately. Dividing very long runs into sections assures that the main axis is properly calculated in case the microtubule exhibits small curvatures. In any case, the principal axis is obtained by rotating the coordinates p_i with the angle

$$\phi = -\frac{1}{2}\arctan\left(\frac{2I_{xy}}{I_x - I_y}\right) \qquad \text{[S2]}$$

resulting in rotated coordinates $q_i = (x_i', y_i')$. We assured that this axis coincides with the microtubule axis by visual inspection. The x'-coordinate involves the processive movement and is termed 'main axis' while y'-coordinate is termed 'perpendicular' axis and contains mostly noise. As a control we additionally calculated the mean squared displacement (MSD) versus time relationship of tacks along the main and perpendicular axis separately; the former yields a parabolic curve while the latter is roughly constant, representing the accuracy limit of ~40 nm (data not shown).

Then, the Pythagorean length d and the vector angle α relative to the main axis of movement were calculated for each frame-to-frame displacement. Displacements with length $d < d_{crit}$ = 40 nm and a vector angle $|\alpha| > \alpha_{crit} = 60°$, e.g. backwards ($\alpha$ = -180°), were classified as 'waiting intervals' (Fig. S3 A, red lines) in contrast to 'moving intervals' (black lines). Subsequently, waiting intervals are combined to whole 'waiting periods'. In the simplest case, a total 'waiting period' consists of several consecutive frame-to-frame waiting intervals (Fig. S3 B, top). However, the noise of the fluorescence signal and its detection allows, in principle, sometimes the measurement of apparent displacements larger than d_{crit} even for the situation that a motor does not change position. Therefore, we allowed isolated 'moving intervals' within waiting periods, as illustrated in Fig. S3 B, bottom. Starting from a first waiting interval (blue circles) we looked for the particular frame for which two or more (dashed rectangle in Fig. S3 B) moving intervals follow, and defined this frame as 'end' of the waiting period (red circles). The duration of the whole waiting period is equal to the total number of frames involved.

Intuitively, one would expect that the net displacement during any waiting period should be close to zero. Therefore, we produced a histogram of the net displacement (distance between blue and red circle in Fig. S3 B) of all detected pauses and stops from pooled data. Displacements along the main and perpendicular axis were analyzed separately. For the main axis a positive bias was found; the mean was 86 nm and the standard deviation was 97 nm and, thus, included the origin (Fig. S3 C). The positive bias is a characteristic of the algorithm working as threshold filter. On the other hand, the mean net displacement along the perpendicular axis is essentially zero (Fig. S3 D). Note that each net displacement involves at least three frames.

Fitting simulated exponentially distributed data with mean T and cut-off τ

Appendix A gives the mathematical basis for mean value estimation of exponentially distributed data with mean $T > 0$ and a lower cut-off $\tau \geq 0$ below which no events are measured ('truncated data'). We determined the dependence of the accuracy of such an estimation on τ by repeatedly simulating data samples and fitting with a shifted exponential according to formula [5], Appendix A. In brief, exponentially distributed data samples ($N_S = 1000$) with mean $T = 0.2$ were generated with the *exprnd* function in Matlab (The Mathworks), and data points below τ were neglected to finally obtain a data histogram as shown in Fig. S6 A. We assume here that the number of events N_S correlates with observation time t_{obs}, and to increase the number of events one has to measure longer times. In total hundred such samples were generated for a specific value of τ, while τ ranged from 0.0 to 0.5; note that the cut-off τ can be larger than the mean value. As a consequence, the number of 'observed' data points N_{obs} (events larger than τ) decreases exponentially (Fig. S6 B, dashed). This reduction can be compensated for by increasing sample size or, equivalently, longer observation time t_{obs} (Fig. S6 B, outlined). Fitting a shifted exponential function to each of these histograms (using non-linear least-squares) gives an estimate for T with corresponding 95% confidence interval. We can assume that the fluctuation of the parameter T is normally distributed, and calculate a mean T and mean confidence interval from the hundred sample fits. The results are then plotted against τ (Fig. S6 C), and this graph serves as theoretical accuracy for a sample with size $N_S = 1000$. Note that the mean value is still estimated correctly although τ is larger than T and events with mean duration are actually never observed. If sample size is not compensated (i.e. t_{obs} = constant, Fig. S6 C) the accuracy decreases with τ (diverging confidence interval). However, in case the number of observations is kept constant ($N_{obs} \approx 1000$) the accuracy remains roughly constant (Fig. S6 D), but the observation time must increase exponentially.

SUPPLEMENTARY REFERENCES

1. Surrey, T., M. B. Elowitz, P. E. Wolf, F. Yang, F. Nedelec, K. Shokat, and S. Leibler. 1998. Chromophore-assisted light inactivation and self-organization of microtubules and motors. Proc Natl Acad Sci U S A 95:4293-4298.
2. Seitz, A. and T. Surrey. 2006. Processive movement of single kinesins on crowded microtubules visualized using quantum dots. EMBO J 25:267-277.
3. Vale, R. D., T. Funatsu, D. W. Pierce, L. Romberg, Y. Harada, and T. Yanagida. 1996. Direct observation of single kinesin molecules moving along microtubules. Nature 380:451-453.

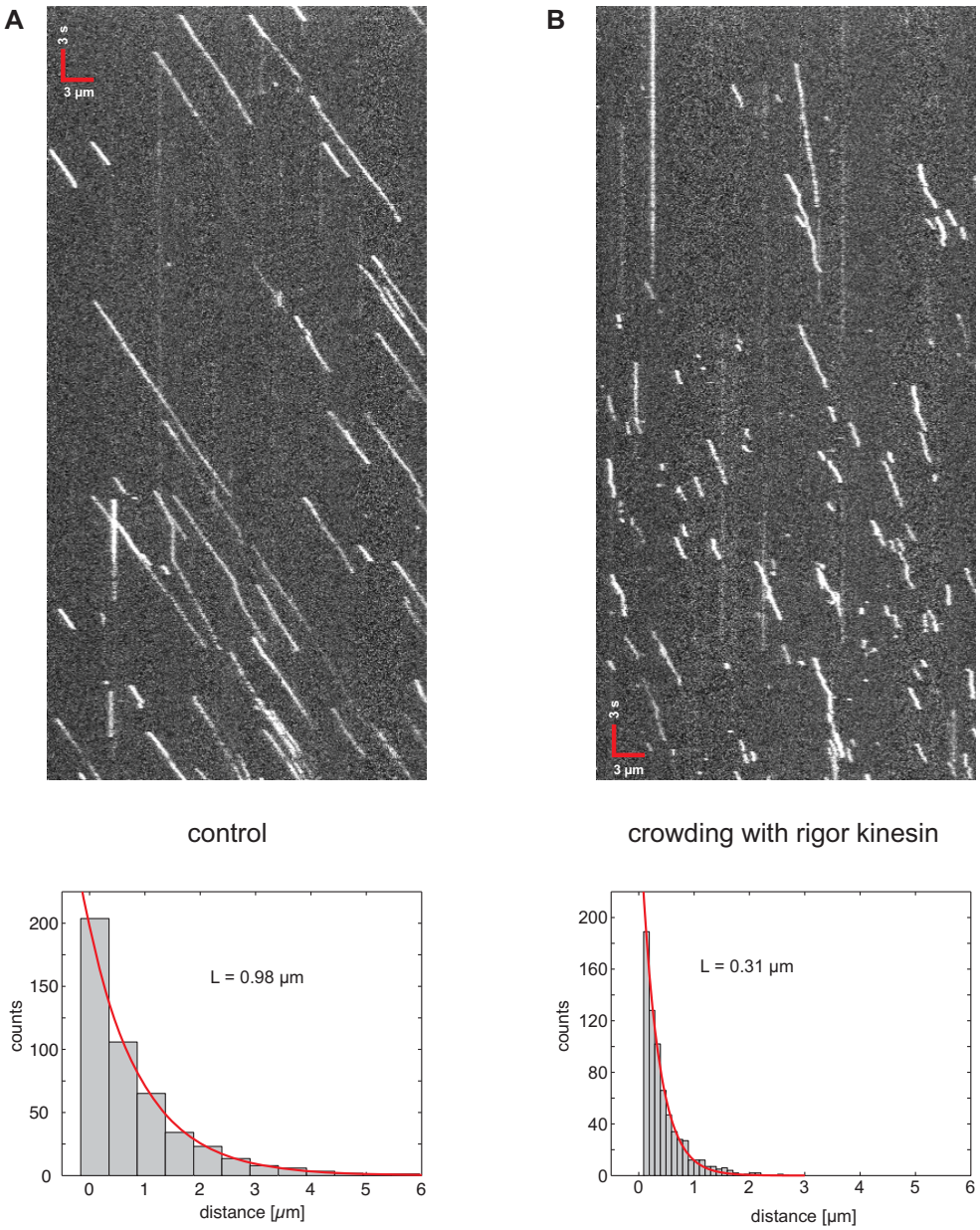

Fig. S1: Surface passivation using β-casein

Data from a single molecule assay with casein blocking and microtubule immobilization by means of rabbit anti-Tub antibody non-specifically adhered to the glass surface. **(A)** Control experiment in which Kin401mGFP alone interacts with microtubules. A sample kymograph (top) illustrates that the run velocity is uniform, and the mean run length (bottom) is in agreement with reported values in the past (3) and is only slightly shorter than the mean value measured with PEG-biotin surfaces. **(B)** Crowding experiment in which rigor kinesin obstruct the runs of processive wildtype kinesin. Microtubules were incubated with 20 nM Kin_{401}[T99N]mCherry with subsequent washing, and Kin_{401}mGFP was added as described in the Suppl. Materials and Methods. A sample kymograph (top) shows that kinesins often pause or stop and that the dwell time is shorter. The run length distribution (bottom) confirms the finding with PEG-biotin glass that the processivity is decreased due to roadblocks. These experiments suggest that the finding of decreased processivity and increased pause frequency under molecular crowding can be reproduced using other surface passivation methods.

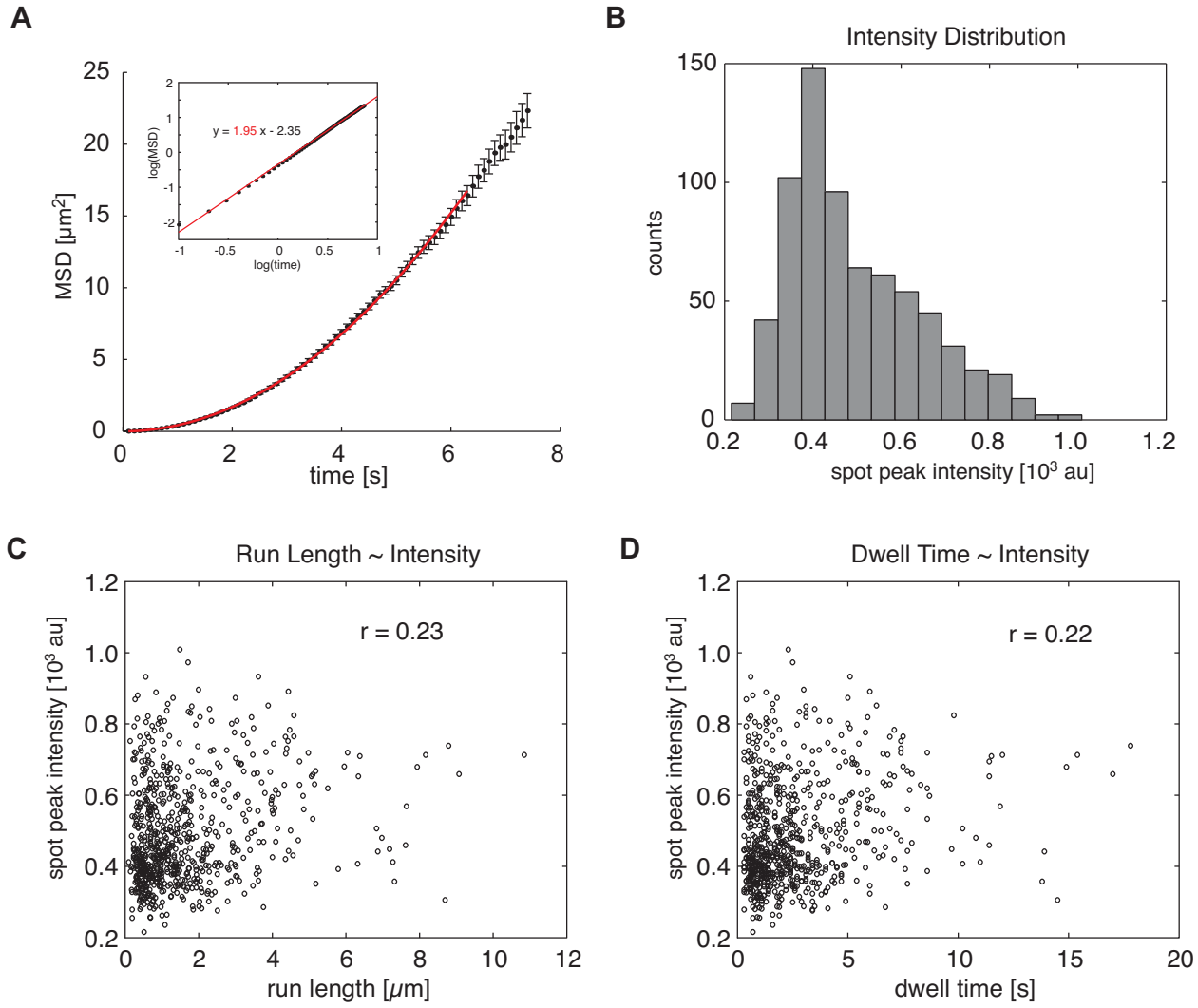

Fig. S2: Velocity and brightness of Kin_{401}mGFP in the control experiment

(A) Plot of the mean squared displacement (MSD) as a function of time of a population of runs (n > 500) from the control experiment. Data points are mean and error bars are S.E.M. The red line represents a fit with the parabolic function $MSD(t) = v^2t^2$ and estimates the unimpeded mean stepping velocity of Kin_{401}mGFP as 0.66 μm/s. Inset: logarithmic plot of the data (dotted) and superimposed linear fit (red line). For perfectly parabolic data a slope of 2 is expected for the linear fit. **(B)** Distribution of the background subtracted peak value of signal spots detected as processive runs, exhibiting a principal mode at ~400 a.u. but also broad right-side tail mostly due to the resolution limit in separation of coincident spots, irregular field flatness of the imaging system, and possibly also minor oligomerization. The dependence of peak intensity on run length **(C)** or dwell time **(D)** did not result in a significant correlation, as suggested by Pearson product-moment correlation coefficient *r* given in the figures.

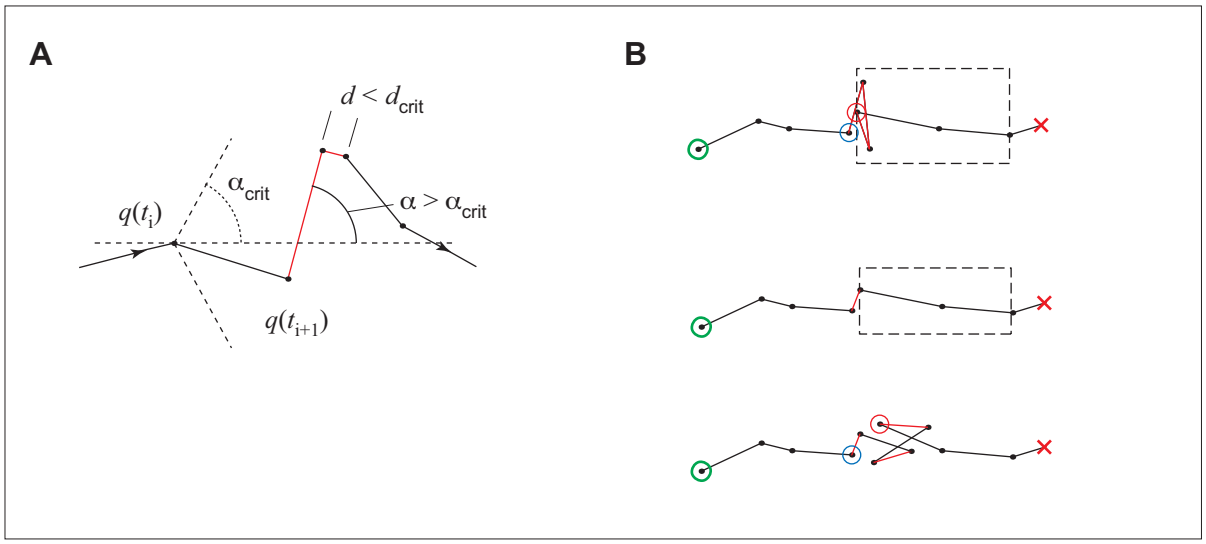

Displacement during waiting periods

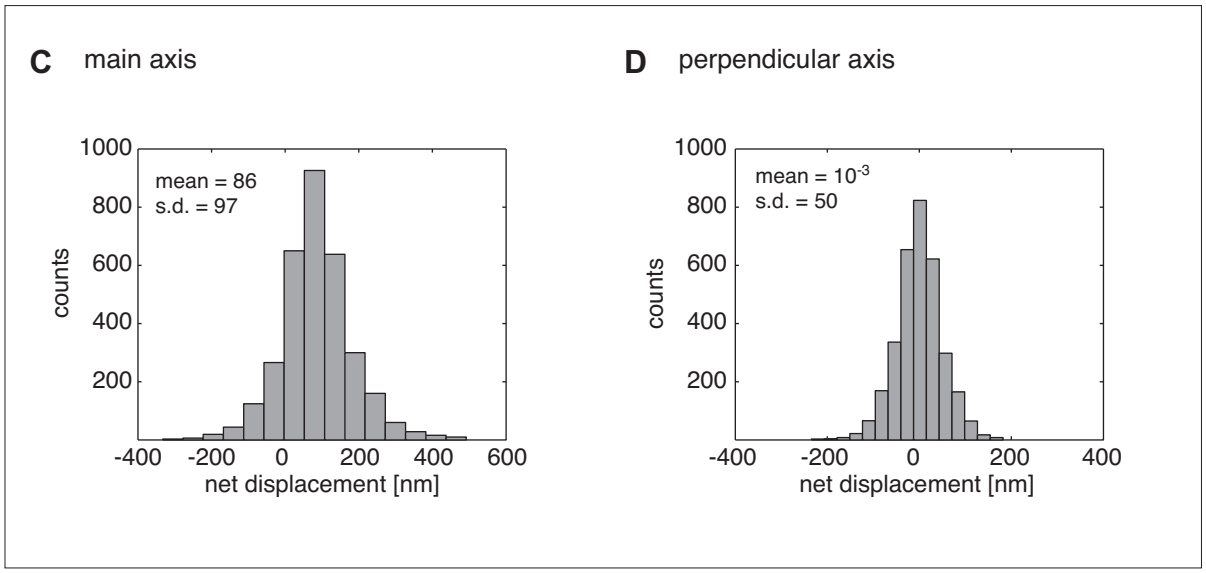

Duration of waiting periods

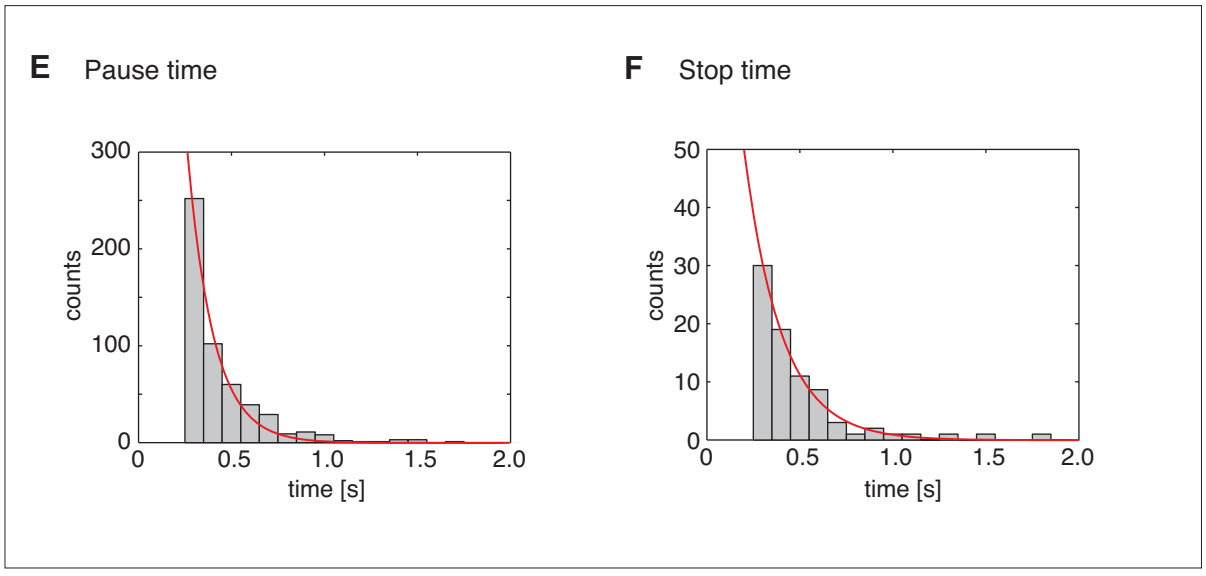

Fig. S3: Detection scheme, net displacement and duration of detected pauses and stops

(A) Detection scheme illustrating the criterions for a particular displacement to be *candidate* for non-processive motion (also termed 'waiting interval' in the text, red lines); (i) the displacement vector x from a frame t to the following frame t+1 exceeds a critical angle α_{crit} relative to the main axis, or (ii) the absolute (pytagorean) length of the vector is below a threshold distance d_{crit}. The arrows indicate the direction of motion. **(B)** Consecutive candidate intervals (red lines) were combined to one single waiting period (top), and were terminated (red circle) when (iii) at least two processive displacements would follow, as indicated by the dashed frame. Short periods involving one or two waiting intervals only were not considered (middle). The third criterion allows single processive displacements in between non-processive intervals (bottom, black lines in between red ones) for reasons of stochasticity. Red and blue circles represent the beginning and end, respectively, of a detected waiting period. **(C)** Histogram of net displacements (distance between blue and red circle as shown in B) for all detected waiting periods (pauses and stops) along the main axis. The positive bias represents the filter characteristics of the detection algorithm using an absolute threshold. **(D)** Histogram of net displacements along the perpendicular axis, representing the fluctuation of the localization from signal noise. For details see Suppl. Methods. The histograms in **(E)** and **(F)** show the distribution of the duration of detected pauses ('pause time') and stops ('stop time'), respectively, with corresponding exponential fit (red). The data was obtained from the experiments with 20 nM wildtype Kin_{401} as crowding agent.

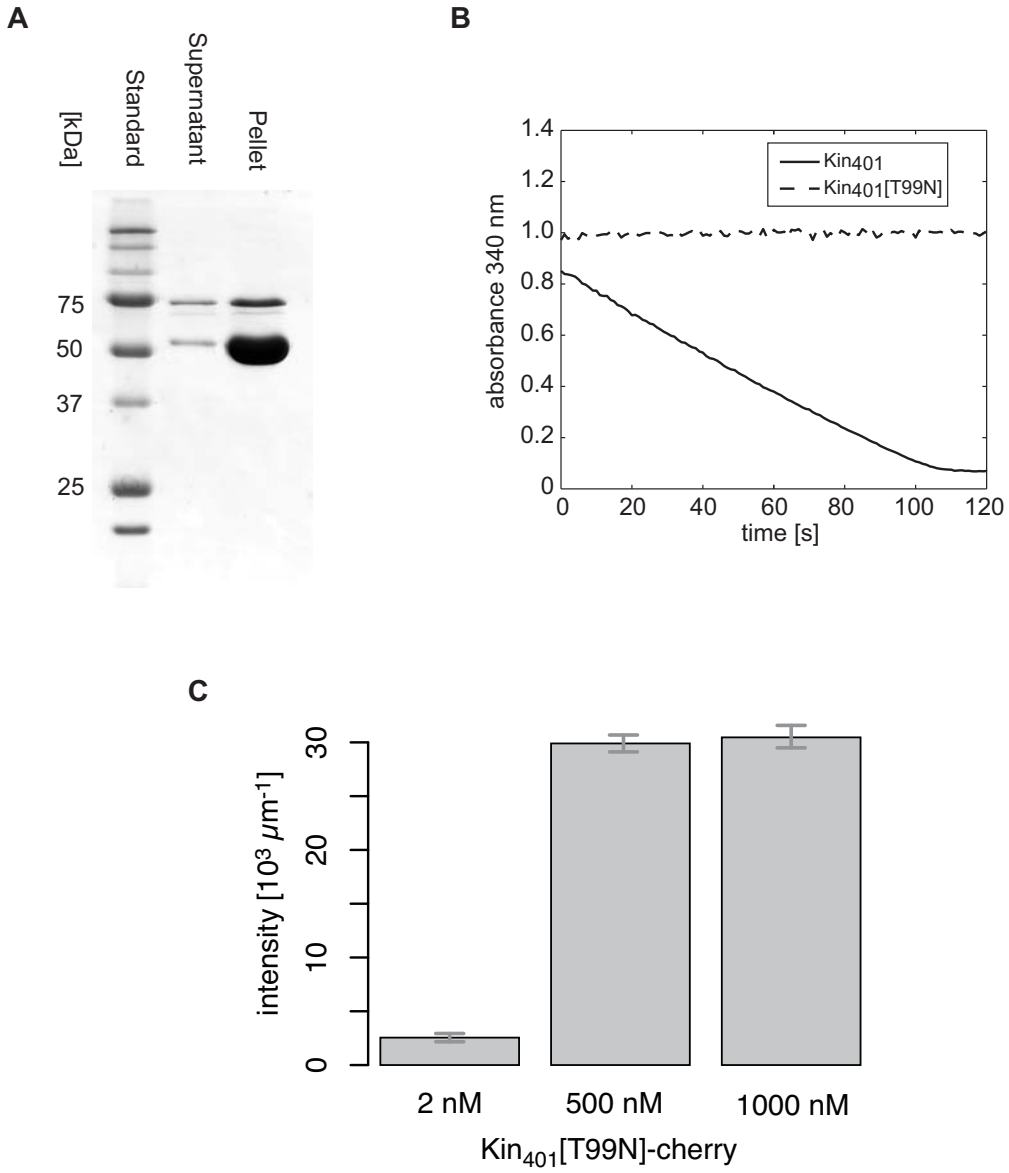

Fig. S4: Biochemical characterization and binding properties of the mutant kinesin Kin_{401}[T99N]

(A) Coommassie stained polyacrylamid gel of the supernatant and the resuspended pellet from a co-sedimentation assay in which taxol-stabilized microtubules and mutant kinesin molecules are mixed and centrifuged at 70'000 rpm for 10 min in assay buffer in the presence of ATP. Microtubules and bound kinesins precipitate while free tubulin and tubulin-associated or free kinesins remain in the supernatant. **(B)** Time course of enzyme-linked ATPase activity of the wild-type kinesin (outlined) and the mutant kinesin (dashed) at a concentration of 50 nM in the presence of 100 nM microtubules at 25 °C. While the wild-type kinesin hydrolyses ATP at the expected rate the mutant kinesin is inactive despite its binding affinity shown in A. **(C)** Microtubule integrated intensity of Kin_{401}[T99N]mCherry determined by TIRF microscopy at the concentrations used for crowding (2 nM) and at two saturating concentrations. The background-subtracted intensity along microtubules was integrated and divided by microtubule length. The measurement suggests that the decoration of the microtubules with mutant kinesin in the crowding experiment was ~8% relative to saturated decoration.

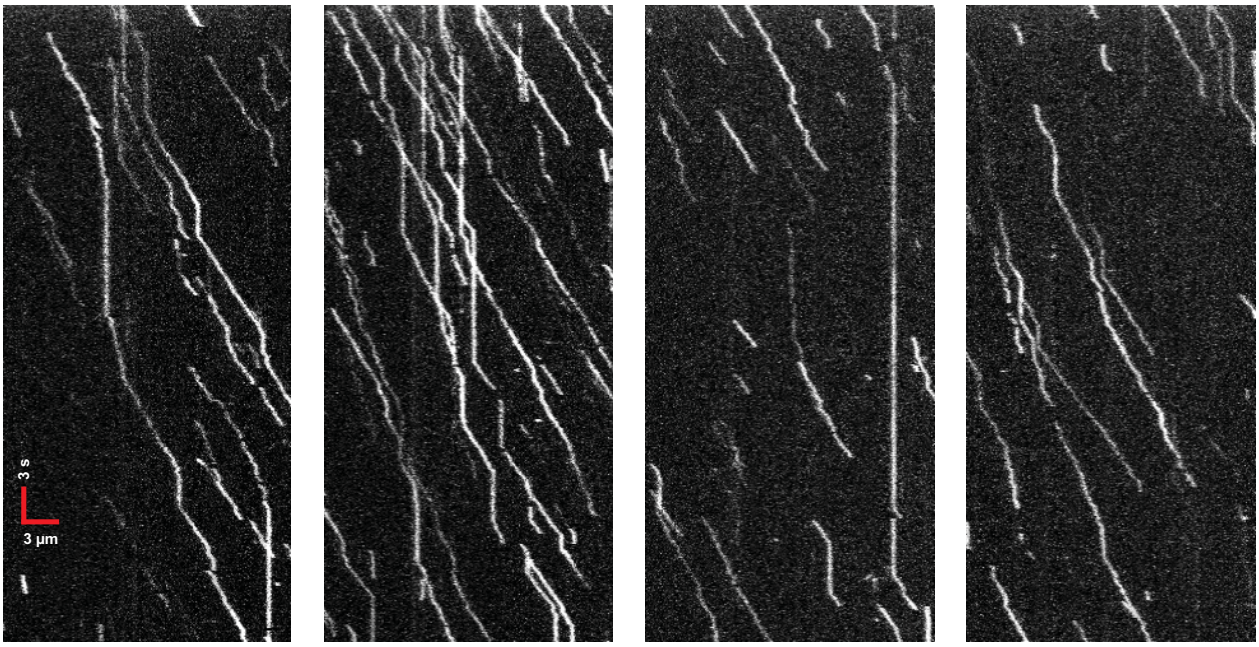

Fig. S5: Crowding experiment using Kin_{401}BCCP-Qdot and rigor Kin_{401}[T99N]

Crowding experiment at the same conditions as in the experiment shown in Fig. S2 B, but using quantum dot labeled kinesin as reporter. Microtubules were first incubated with 20 nM Kin_{401}[T99N]mGFP, washed thereafter, and biotinylated wildtype kinesin Kin_{401}BCCP coupled to streptavidin coated quantum dots (Qdot 585 nm) were added and imaged by TIRF microscopy. Sample kymographs show that in contrast to GFP-labeled kinesins, which showed short runs (Fig. S2 B), the Qdots were carried over long distances and exhibited pauses in the range of seconds. This experiment suggests that the processivity of Qdot labeled kinesins is less affected by obstacles, presumably because quantum dots interact non-specifically with the obstacle or the microtubule.

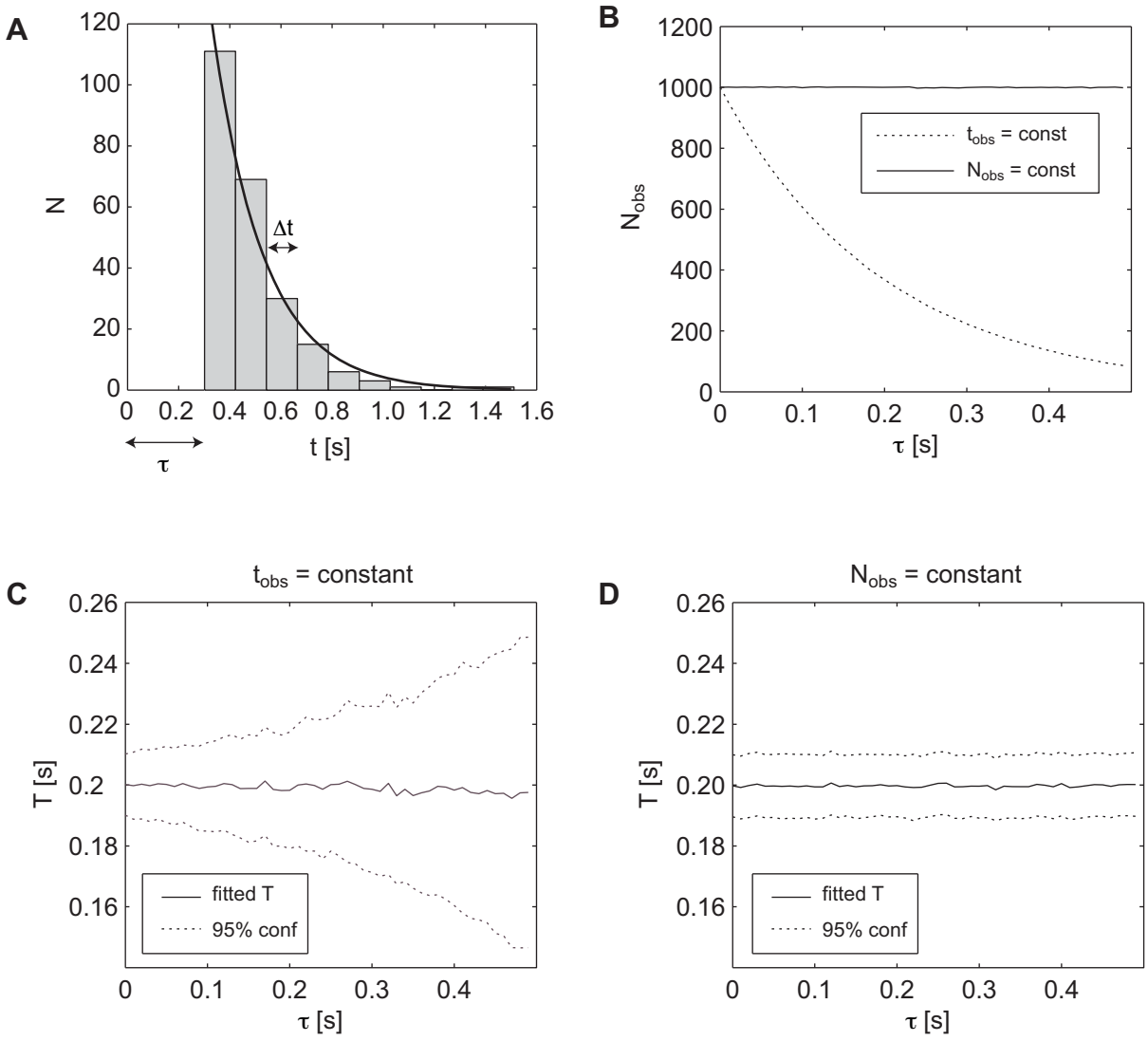

Fig. S6: Simulation of the theoretical accuracy when fitting exponential distributions suffering a lower cut-off

(A) Histogram of randomly generated sample data with bin size Δt, mean value $T = 0.2$ and cut-off $\tau = 0.3$. The thick line denotes the corresponding fit of the histogram. **(B)** Dependence of the number of observed events N_{obs} on the lower cut-off τ. For a constant observation time t_{obs} the number of observations N_{obs} decreases with increasing cut-off τ; this can be compensated for by observing longer times (outlined). **(C)** Computed mean value T and corresponding 95% confidence interval plotted against τ for a constant observation time. **(D)** Computed mean value T and corresponding 95% confidence interval plotted against τ for a constant number of observed events. For details see Suppl. Materials and Methods.